Shape evolution of droplet impingement dynamics in Ink-Jet manufacturing

Wenchao Zhou, Drew Loney, Andrei G. Fedorov, F. Levent Degertekin, David W. Rosen

The George W. Woodruff School of Mechanical Engineering, Georgia Institute of Technology,
813 Ferst Drive, Atlanta, GA, 30332-0405, USA

REVIEWED, August 17 2011

Abstract

Ink-jet printing enables more efficient, economic, scalable manufacturing for a wide variety of materials than other traditional additive techniques. The impact of droplets onto a substrate is critical for accuracy control and optimization of the droplet deposition process. However, most previous research about droplet impact focused on the spreading radius of the droplet, which does not provide enough information for manufacturing purposes. This paper presents new methods to model and characterize droplet shape change during impact so that the droplet deposition process can be optimized to build desired geometries. A validated numerical model is used to study the shape change of the droplet impingement on a solid surface. A dimensional analysis is conducted to reduce the number of parameters of the impact conditions by matching Reynolds, Weber, and Froude numbers as well as possible. In addition, a new method of characterizing droplet shape is presented that measures its similarity to a desired shape. The shape evolution of a wide range of impact conditions is simulated with the validated numerical model using both physical and dimensionless quantities. The effects of the dimensionless numbers on the shape evolution are examined and analyzed. Successive multiple droplets impact is also simulated.

1. Introduction

Ink-jet printing is an emerging technology that provides a more efficient, economic, scalable method of manufacturing than other additive techniques. A good understanding of the underlying physics of droplet impingement onto a substrate is critical for accuracy control and optimization of the deposition process. Although the interaction of drops with surfaces has been extensively and intensively investigated for over a century [1], the development of comprehensive, predictive models has been difficult due to the complexity of the process and the interactions among many physical phenomena, including fluid mechanics, phase change, and surface chemistry. Nevertheless, numerous research progresses have been reported during the past century. The contact angle hysteresis phenomenon was also observed [2] and analyzed [3-4]. Experimental studies have been performed on the time evolution of droplet shape on a solid surface [5] and on impact regimes based on the combination of driving forces and resisting forces to simplify the problem [6]. Splash phenomena have also been studied, different causes for splash have been found [1, 7-9], and suggestions for avoiding splash have been proposed, all of which are essential for ink-jet manufacturing. Different theoretical models [10-11] and numerical models [12-16] have been proposed.

However, most of the previous research focused on studying the change of a single variable -- the droplet spreading radius, which cannot provide enough information for manufacturing purposes. This paper presents a new measure to characterize droplet shape change during impact so that the droplet deposition process can be optimized to build desired geometries. With the new measure of droplet shape characterization, a dimensional analysis is first conducted to reduce the number of parameters of the impact conditions. Then a wide range of impact conditions are simulated with a validated numerical model [17]. Results show that it is possible to track the evolving shape of a deposit formed by multiple droplets.

The rest of the paper is organized as follows. In section 2, a measure of droplet shape characterization is presented. Section 3 gives a dimensional analysis of droplet impingement dynamics. In section 4, droplet impact under a wide range of impact conditions is simulated and the droplet size effects are presented. Section 5 is devoted to studying effects of dimensionless numbers on the shape evolution of droplet impact while successive droplets impact under ideal conditions are investigated in section 6. Conclusions are given in section 7.

2. Droplet Shape Definition

In order to build the desired geometry, it is desirable to optimize the droplet impact conditions so that desired geometries can be fabricated. To accomplish this, the shape evolution of droplets during impingement needs to be characterized and compared with the desired geometry. The many methods of shape representation can be categorized generally into contour-based methods and region-based methods [18]. In this paper, the contour based shape representation method is used. To characterize the droplet shape, the contour of the droplet is obtained from the simulation using image processing techniques; a resulting droplet cross section is shown in Figure 1.

With the contour, we can get the coordinates of the points on the contour, which are (x(j), y(j), where j=1,2,...N). The centroid distance is used to represent the shape of the droplet as a shape signature, which is defined as the distance between the boundary points and the centroid of the droplet shape. The centroid is calculated by:

$$x_c = \frac{1}{N}\sum_{j=1}^{N} x_i \; ; \; y_c = \frac{1}{N}\sum_{j=1}^{N} y_i \tag{1}$$

The centroid distance is defined as:

$$r(j) = \sqrt{(x(j) - x_c)^2 + (y(j) - y_c)^2} \tag{2}$$

To overcome the problem of noise sensitivity, a Fourier transform is applied to the centroid distance vector r:

$$R(k) = \frac{1}{N}\sum_{j=1}^{N} r(j) e^{2\pi i(j-1)(k-1)/N} \tag{3}$$

The vector R can be used to characterize the droplet shape. In the same way, we can define a vector RR to characterize the desired geometry. In this paper, the desired geometry is set to a uniform film (i.e., a rectangle in 2D). For uniformity, we define a rectangle that includes the droplet as shown in Figure 1.

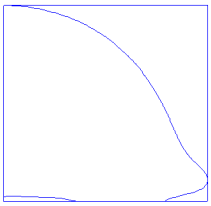

Figure 1 Droplet included by a rectangle

The similarity between the droplet shape and the desired geometry can be evaluated by the Euclidean distance between the two shape vectors R and RR, representing the simulated and the desired droplet shapes, respectively. Therefore, a similarity coefficient 'R-Coefficient (RC)' can be defined to measure how close the droplet shape is to the desired shape:

$$RC = 1 - \sqrt{\sum_{j=1}^{N} (R(j) - RR(j))^2} \Big/ \sqrt{\sum_{j=1}^{N} RR(j)^2} \tag{4}$$

The R-coefficient ranges from 0 to 1 and 1 means the perfect match between the droplet shape and the desired geometry. Figure 2 shows how the R-coefficient is correlated with the droplet shape and how it changes with time. It can be seen that the R-coefficient correctly characterized the similarity between the droplet shape and the desired geometry.

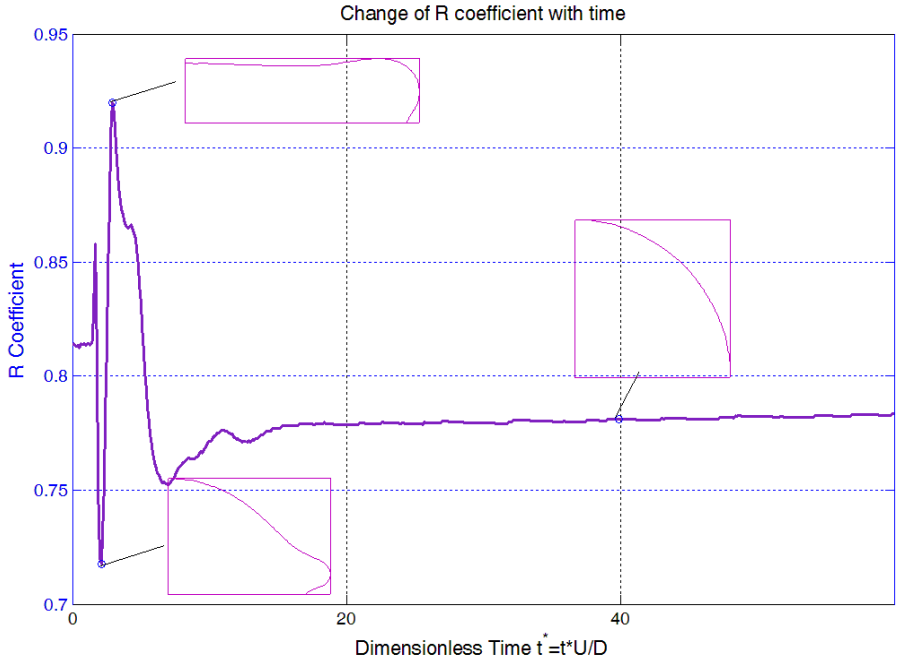

Figure 2 Change of R-coefficient during the droplet impingement

3. Dimensionless Analysis

To understand the effects of different fluid parameters on droplet impingement, a dimensionless analysis is performed on the numerical model [17]. The phase-field method is used and the governing equations are:

$$\rho\frac{\partial u}{\partial t}+\rho(u\cdot\nabla)u=\nabla\cdot[-pI+\eta(\nabla u+(\nabla u)^T)]+\rho g+G\nabla\phi \tag{5.a}$$

$$\nabla\cdot u=0 \tag{5.b}$$

$$\frac{\partial\phi}{\partial t}+u\cdot\nabla\phi=\nabla\cdot\left(\frac{\gamma\lambda}{\varepsilon^2}\right)\nabla\varphi,\lambda=\frac{3\varepsilon\sigma}{\sqrt{8}},\gamma=\chi\varepsilon^2 \tag{5.c}$$

$$\varphi=-\nabla\cdot\varepsilon^2\nabla\phi+(\phi^2-1)\phi \tag{5.d}$$

$$\sigma=\frac{2\sqrt{2}\lambda}{3\varepsilon},G=\frac{\lambda\varphi}{\varepsilon^2} \tag{5.e}$$

where ρ is the fluid's density (kg/m3); u is the velocity vector (m/s); p represents the pressure (Pa); η denotes the dynamic viscosity (Pa · s); γ is the mobility (m^3·s/kg), λ is the mixing energy density (N), ϕ is a dimensionless phase parameter and ε (m) is the interface thickness parameter.

The physical parameters can be nondimensionalized with respect to the reference physical parameters:

$$u^*=\frac{u}{U};\ t^*=\frac{tU}{L};\ x^*=\frac{x}{L};\ p^*=\frac{p}{\rho_{ref}U^2};\ g^*=\frac{g}{g_{ref}};$$

$$\rho^*=\frac{\rho}{\rho_{ref}};\eta^*=\frac{\eta}{\eta_{ref}};\ \sigma^*=\frac{\sigma}{\sigma_{ref}};\mathrm{G}^*=\mathrm{G}\frac{\rho_{ref}U^2}{\sigma_{ref}}$$

where * stands for dimensionless, the subscript 'ref' denotes the reference parameter.

Then equation (5.a) can be rewritten as:

$$\rho_{ref}\rho^*\frac{U\partial u^*}{L}+\rho_{ref}\rho^*\left(Uu^*\cdot\frac{\nabla^*}{\mathrm{L}}\right)Uu^*=$$

$$\frac{\nabla^*}{\mathrm{L}}\cdot\left[-\rho_{ref}U^2p^*I+\eta_{ref}\eta^*\left(\nabla^*\mathrm{u}^*\frac{U}{L}+\frac{U}{L}(\nabla^*\mathrm{u}^*)^T\right)\right]+\rho_{ref}g_{ref}\rho^*g^*+G^*\frac{\sigma_{ref}}{\rho_{ref}U^2}\frac{\nabla^*}{\mathrm{L}}\phi \tag{6.a}$$

Rearranging equation (6.a), we have

$$\rho^* \frac{\partial u^*}{\partial t^*} + \rho^*(u^* \cdot \nabla^*)u^* = \nabla^* \cdot \left[-p^* I + \frac{1}{Re}\eta^*(\nabla^* u^* + (\nabla^* u^*)^T)\right] + \frac{1}{Fr}\rho^* g^* + \frac{1}{We} G^* \nabla^* \phi \quad (6.b)$$

where, $\mathrm{Re} = \frac{\rho_{ref} U L}{\eta_{ref}}$; $\mathrm{We} = \frac{\rho_{ref} U^2 L}{\sigma_{ref}}$; $\mathrm{Fr} = \frac{U^2}{L g_{ref}}$.

Based on this analysis, the solutions of the governing equations under different impact conditions will be the same as long as these three dimensionless numbers match with each other (The contact angle between droplet and solid surface is limited to π/2 in this paper). Therefore, instead of dealing with 6 physical parameters, we can focus on these 3 dimensionless numbers. A numerical simulation is performed using this numerical model with both the physical parameters and their corresponding dimensionless numbers, which are listed as in Table 1.

Table 1 Dimensionless parameters and physical parameters

Dimensionless Parameters	Physical parameters
u^*=-1	u=--10m/s
ρ_{ink}^*=1	ρ_{ink}= 1000 kg/m^3
ρ_{air}^* = 0.0012	ρ_{air}= 1.225 kg/m^3
η_{ink}^*=1	η_{ink} = 0.01 Pa*s
η_{air}^* = 0.0017984	η_{air} = 1.7894e-5 Pa*s
σ^* = 1	σ = 0.07 N/m
g^* = 1	g = 9.81 m/s^2
D = 1	D = 50e-6 m
Re = 50	
We = 69.4734	
Fr = 2.0387e5	
$\eta_{ink} = \eta_{ink}^*$/Re = 0.02	
$\eta_{air} = \eta_{air}^*$/Re = 3.6e-5	
$\sigma = \sigma^*$ / We = 0.0144	
$g = g^*$ / Fr = 4.905e-6	

The simulation results are compared as shown in Figure 3 and Figure 4. It can be seen that the results in dimensionless domain match well with the results in the physical domain.

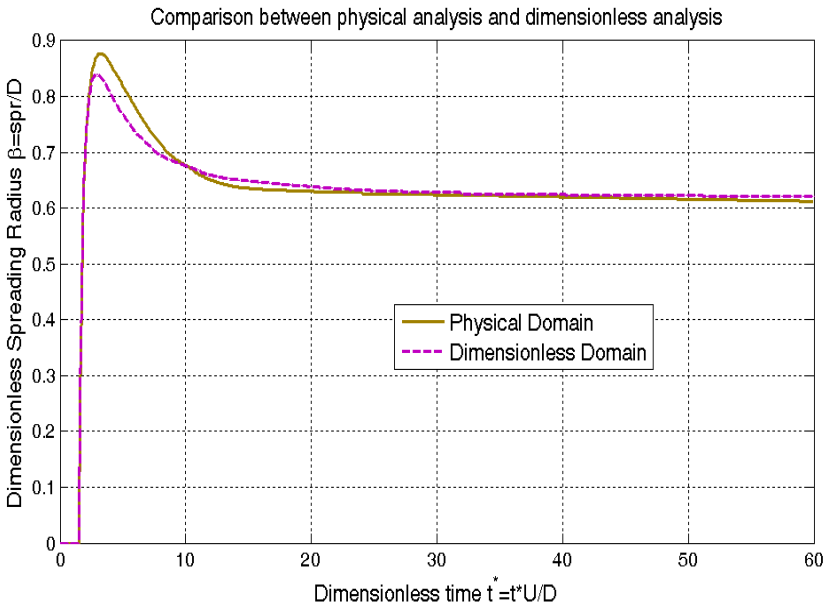

Figure 3 Comparison of spreading radius change between physical domain and dimensionless domain

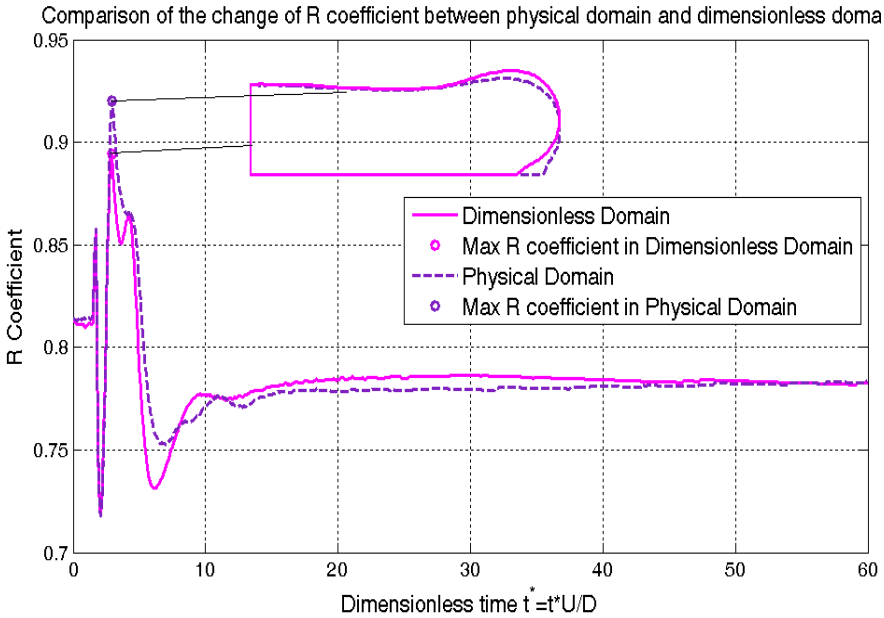

Figure 4 Comparison of R-coefficient change between physical domain and dimensionless domain

4. Droplet impact under different impact conditions

This section is devoted to studying the droplet impact behavior under different impact conditions, i.e. different combinations of the dimensionless numbers, so that we can know how to control the impact conditions to make the droplet shape closer to the desired shape. According to [6], the droplet impact behavior is mainly determined by the driving force and resisting force of the impact and can be divided into four different impact regimes as shown in Figure 5. The Weber number can be used to characterize the driving force and the Ohnesorge number, obtained from the rearrangement of Reynolds number and Weber number ($Oh=(We)^{1/2}/Re$), can be used to characterize the resisting force.

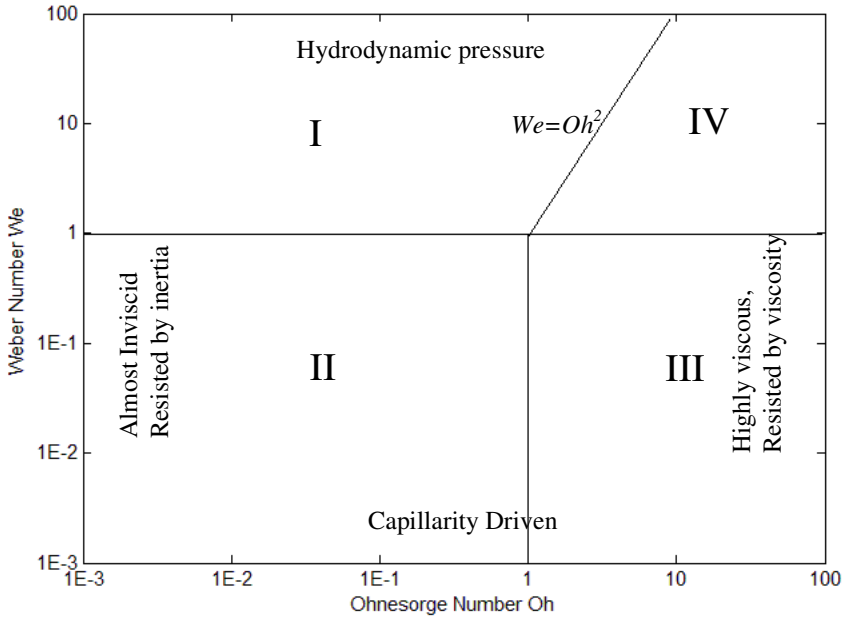

Figure 5 Regime map for the spreading (redrawn based on [6])

Another way to define Weber number and Ohnesorge number is to define them as a ratio of different timescales. There are three different timescales during droplet impingement: spreading timescale τ_{spr} , oscillation timescale τ_{osc} and viscous timescale τ_{vis}:

$$\tau_{spr} = \frac{D}{u};\ \tau_{osc} = \sqrt{\frac{\rho D^3}{\sigma}};\ \tau_{vis} = \frac{\rho D^2}{\eta}. \tag{7}$$

Weber number can be defined as a ratio of oscillation timescale to spreading timescale while Ohnesorge number can be defined as a ratio of oscillation timescale to viscous timescale:

$$We = (\frac{\tau_{osc}}{\tau_{spr}})^2; Oh = \frac{\tau_{osc}}{\tau_{vis}}. \tag{8}$$

The impact behaviors are simulated in the four different regimes. In regime I, spreading is driven by the impact pressure and resisted by inertia. In the simulation, the Weber number and the Ohnesorge number are 100 and 0.01 respectively. The change of spreading radius and the R-coefficient with time are plotted as shown in Figure 6. As can be seen, the aspect ratio of the optimal droplet shape is very low, which would result in a lower manufacturing resolution than the droplet size. In addition, the oscillation is expected due to the small Ohnesorge number (i.e. oscillation timescale is smaller than viscous timescale), and oscillations are across one dimensionless time unit because Weber number is larger than 1 (i.e. oscillation timescale is larger than spreading timescale).

Another important observation that can be made is the maximum R-coefficient is achieved before the droplet achieves its maximum spreading radius as shown in Figure 6. This relationship holds true for all the regimes as verified in the following. One possible reason is as follows. Upon impact, the droplet goes away from its equilibrium shape (i.e. sphere-like cap or sphere) after it hits the substrate and the spreading is driven by the hydrodynamic pressure (which is defined as the pressure difference in Bernoulli's equation) and spreading starts to decelerate due to the resistance of viscous and capillarity forces. Before the speed of contact line reaches 0 (i.e. the maximum spreading radius), the capillarity force outweighs the hydrodynamic pressure and dominates the spreading and thus starts to restore the droplet shape back to its equilibrium shape. Since usually the R-coefficient is achieved when the droplet is furthest away from its equilibrium shape.

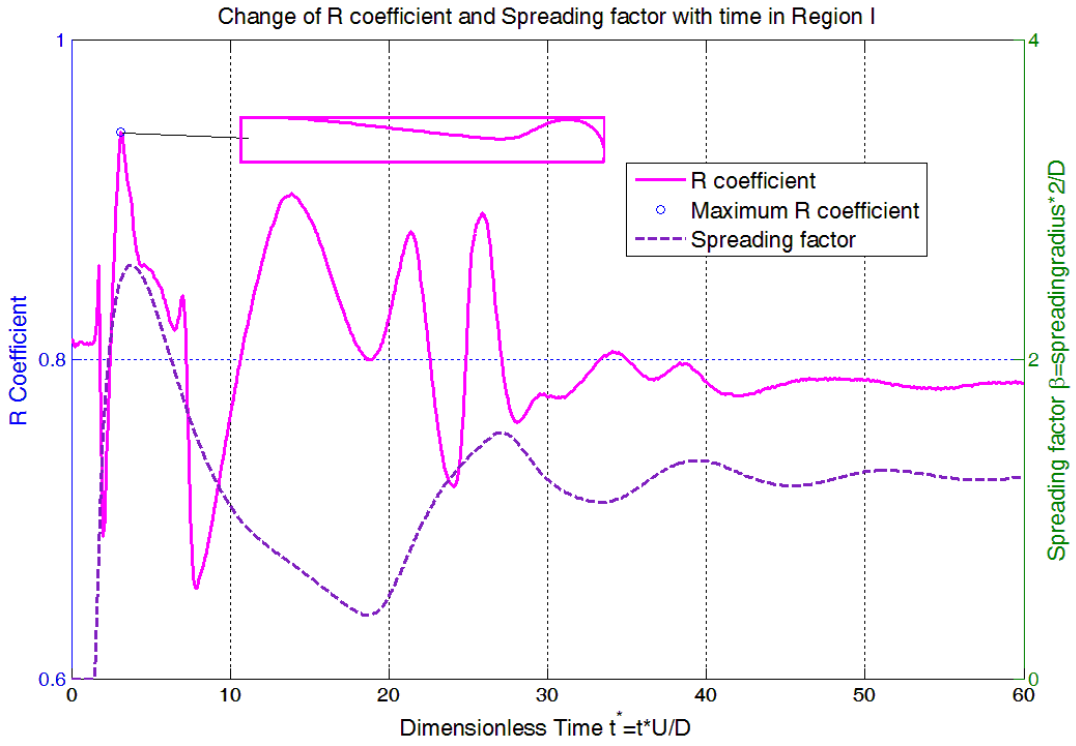

Figure 6 Change of spreading factor and R-coefficient with time in Regime I

In the second region, spreading is mainly driven by the capillarity force imbalance at the contact line since the impact velocity is so slow that its effects can be neglected. Inertia resists spreading, which is followed by under-damped oscillation. In the simulation, the Weber and Ohnesorge numbers are 0.01 and 0.01 respectively and the results are shown in Figure 7. As can be seen, the aspect ratio of the optimal droplet shape is relatively high, which could lead to a better manufacturing resolution than the droplet size. This suggests that the aspect ratio of the droplet shape can be changed by changing the Weber number while keeping the Ohnesorge number the same. Besides, oscillation exists because the Ohnesorge number is smaller than 1 and oscillations disappeared after one dimensionless time unit because the Weber number is smaller than 1. In addition, the relationship that the maximum R-coefficient comes before maximum spreading radius still holds true as shown in Figure 7 although in this regime the two points are very close to each other because the Weber number is so small that the capillarity force dominates the spreading from the beginning.

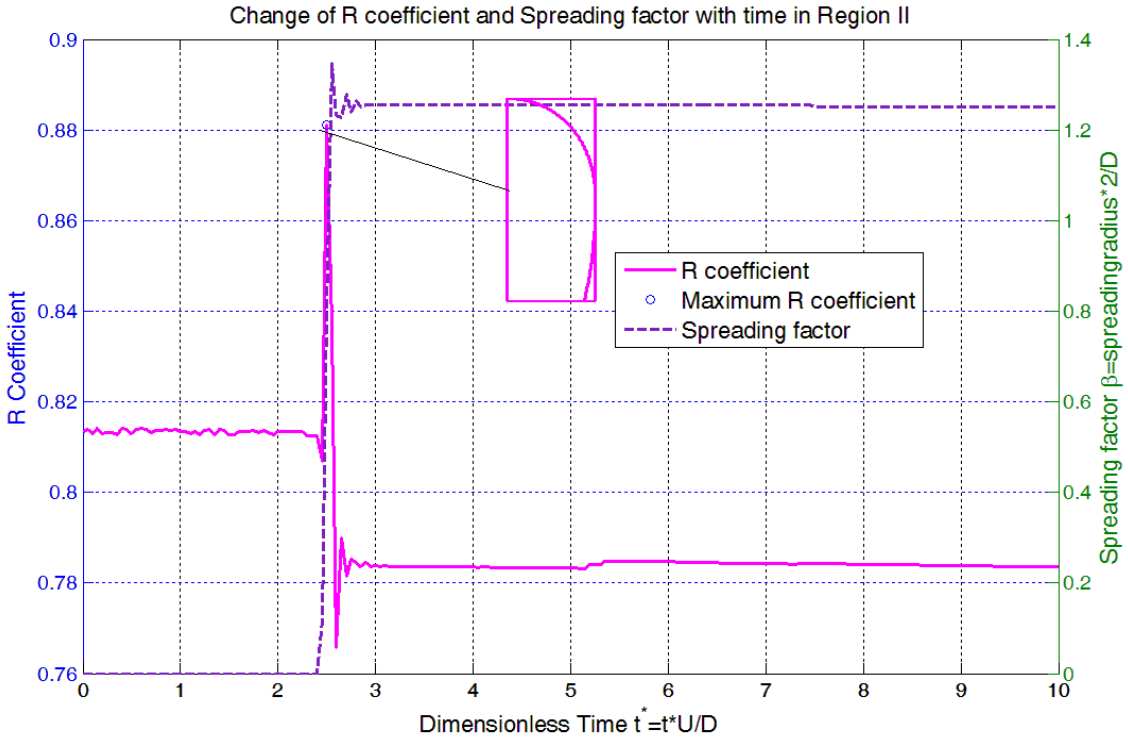

Figure 7 Change of spreading factor and R-coefficient with time in Regime II

In the third region, spreading is driven by the capillarity force and is over-damped by the viscous force so that the inertial oscillations are absent. We simulated droplet impingement with a Weber number of 1 and an Ohnesorge number of 10. The results are shown in Figure 8. As can be seen, the droplet shape starts to change once it hits the substrate, while the spreading radius does not change much until a much later stage. Once again, this confirms that the R-coefficient can show smaller and more detailed change during the impingement process. In addition, the optimal droplet shape does not go very far away from its equilibrium shape due to the high viscous force. Furthermore, the sphere-like shape is likely to cause voids in the parts during the manufacturing process and thus is not a desirable shape, and the impingement process also goes much slower which would lead to longer manufacturing time. Besides, the viscous timescale is smaller than oscillation timescale (Ohnesorge number is larger than 1) and thus the oscillation is damped out. As the same as before, the maximum R-coefficient comes before the maximum spreading radius as shown in Figure 8.

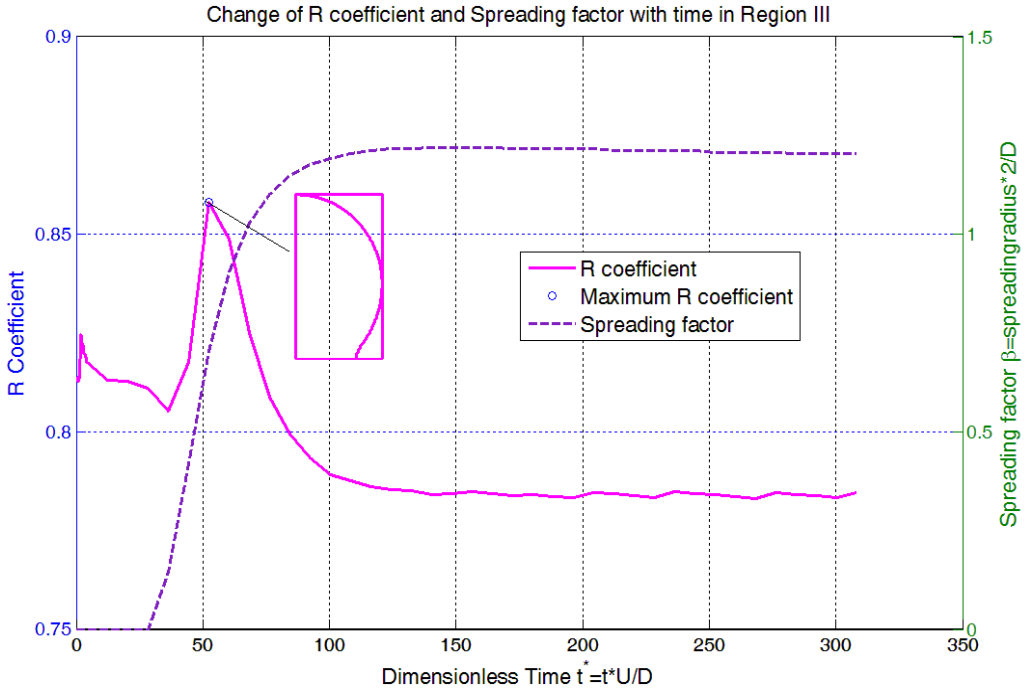

Figure 8 Change of spreading factor and R-coefficient with time in Regime III

In the fourth region, the impact pressure drives the spreading and the viscous force over-damps the spreading so that no oscillation happens. The Weber number and the Ohnesorge number are both 100. The simulation results are shown in Figure 9. As the same as in regime III, the high viscous force and the low inertial energy significantly increase the spreading time and thus the manufacturing time and therefore is not a desirable regime for ink-jet printing. This regime also gives the same relationship between R-coefficient and maximum spreading radius.

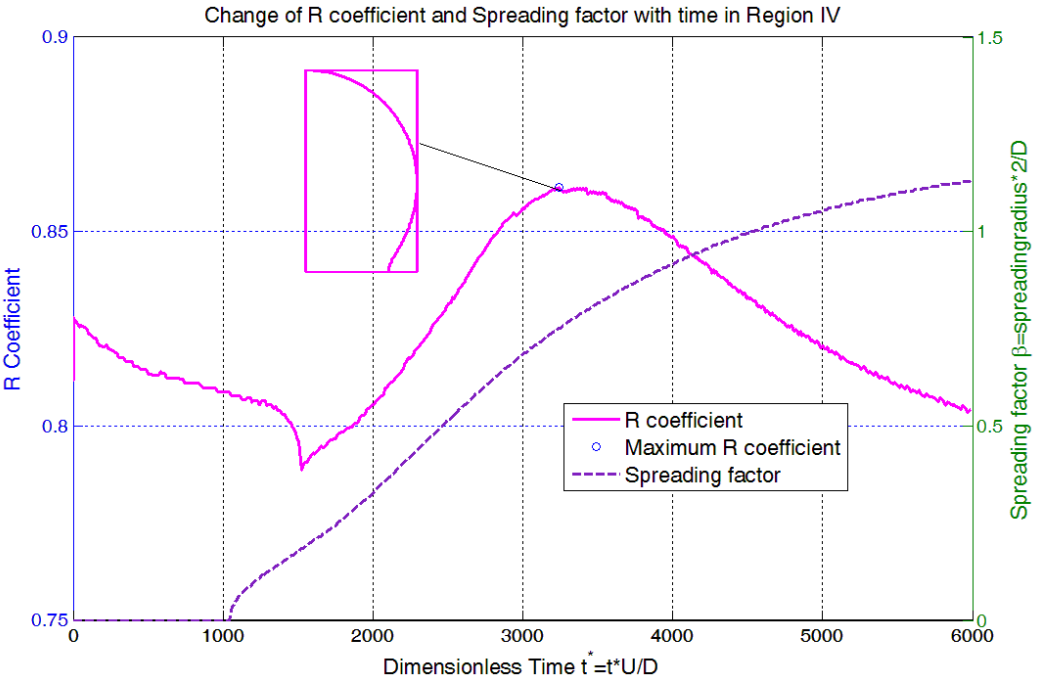

Figure 9 Change of spreading factor and R-coefficient with time in Regime IV

From the above simulation results, we can see that the spreading factor gives us less related information about the droplet shape for manufacture purpose while the R-coefficient can better characterize the droplet shape and give us more information about how to get the desired shape by controlling the impact conditions.

In the regime map in Figure 5, the Froude number derived from the dimensionless analysis was not included. Therefore, a set of simulations was conducted with various Froude numbers and the same Weber number and Reynolds numbers to see the effects of the Froude number on droplet impact behavior. Another reason for doing this is for the purpose of experimentation since it is difficult to conduct experiment at the micro-scale and it is not easy to match up all the three dimensionless numbers at the same time when experiments are conducted at larger size scales.

Our interested material is SR351 resin (a photopolymer with fast cure response and numerous applications) [19] and the material properties at 25oC are listed in Table 2.

Table 2 Material properties of the simulation

Medium	Density	Dynamic Viscosity	Surface Tension
SR351	1.109e3 kg/m^3	0.106 Pa*s	0.0361 N/m
Air	1.1839 kg/m^3	1.8616E-5 Pa*s	

We are interested in the impact behavior of SR351 droplets at micro-scale for potential ink-jet printing application. The Weber and Ohnesorge numbers are set to be 153.6 and 2.37 respectively. The material properties are as listed in Table 2 and the droplet diameter is 50μm. The Weber and Ohnesorge numbers are matched up when the droplet size is scaled up to 200μm, 600μm and 1mm by changing the impact velocity and material viscosity correspondingly as shown in Table 3. The simulation results are compared as shown in Figure 10 and Figure 11.

Table 3 Impact conditions with different droplet size

Droplet Diameter	Corresponding Impact velocity	Corresponding Viscosity
50μm	10m/s	0.1060 Pa*s
200μm	5m/s	0.2120 Pa*s
600μm	2.8868m/s	0.3672 Pa*s
1mm	2.2361m/s	0.4740 Pa*s

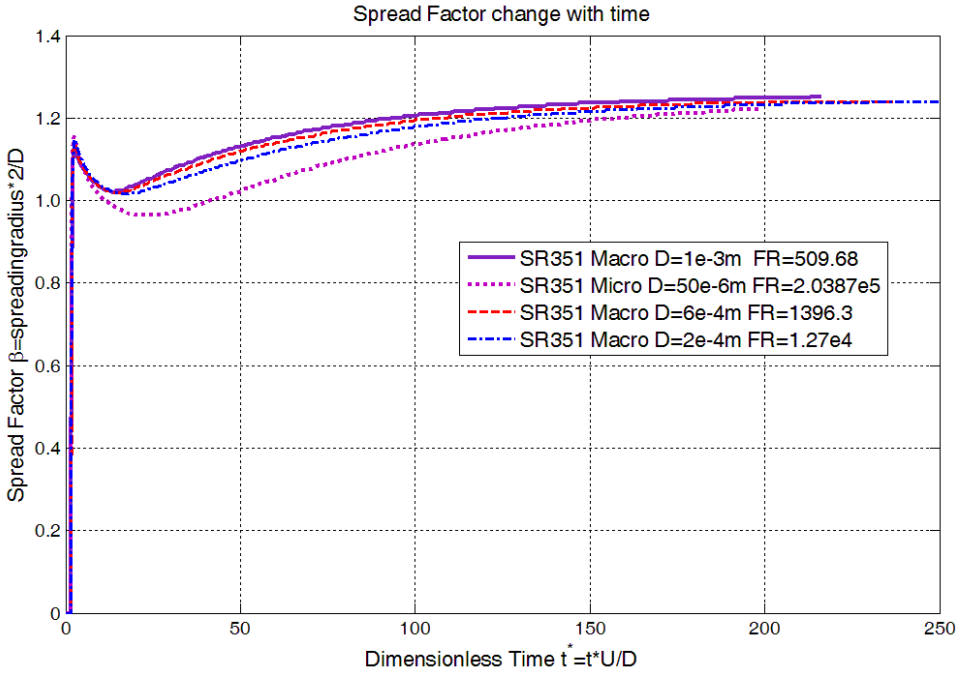

Figure 10 Spread Factor change with time for different droplet size

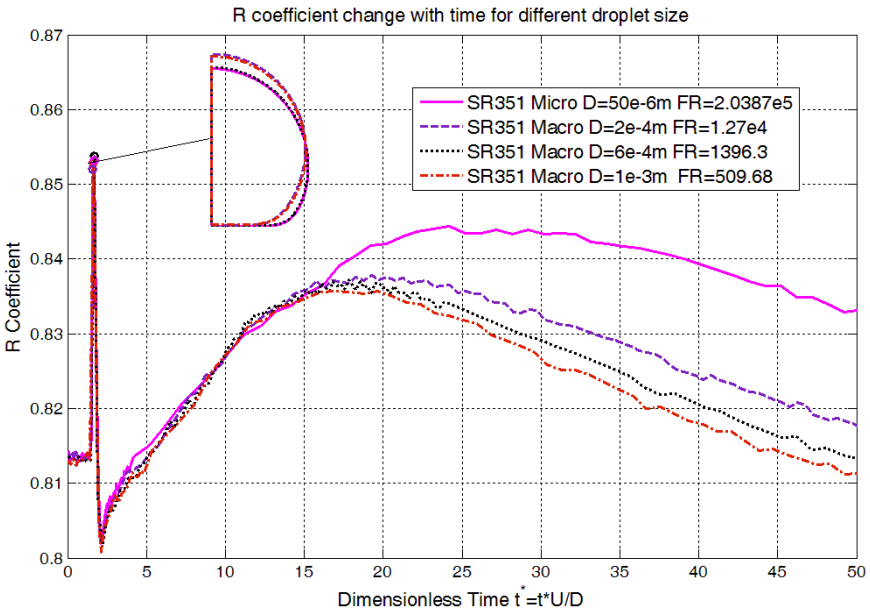

Figure 11 R-coefficient change with time for different droplet size

As shown in the figures, the Froude number does not affect the droplet impact behavior much (the discrepancies in the late stage of the impingement do not matter much since we care about the time range around the maximum R-coefficient), which suggests that the regime map is effective in characterizing droplet impact behavior and it is possible to conduct the experiment in macro-scale to get an estimate of the droplet impact behavior in micro-scale. This can be further confirmed by comparing Froude number with Weber and Ohnesorge numbers. We can see that in the above simulated impact conditions, the Froude number is over 500 (for droplet size of 1mm), which is much higher than Weber number (153.6) and Ohnesorge number (2.37). Referring back to the dimensionless analysis in section 3 (Equation (6.b)), the contribution of Froude number is much less than that of Weber number and Ohnesorge number.

5. Effects of Weber number and Ohnesorge number

This section is devoted to investigating how the Ohnesorge number and Weber number affect the shape evolution of a single droplet, which includes the shape evolution pattern and the time point when the maximum R-coefficient is achieved. Timing control is very important for manufacturing and can help reduce the manufacturing time and thus the manufacturing cost while potentially improving part quality.

1. Effects of Weber number

In order to study the effects of Weber number on the droplet shape evolution, a number of simulations was conducted with parameters listed in Table 4. All the parameters are kept constant except the impact velocity, which is varied from 0.5m/s to 20m/s. To avoid the influence of the viscous force (i.e. to make the viscous force small enough so that the role of Weber number in the shape evolution can be studied), the Ohnesorge number is kept at 0.0813 while the Weber number changes from 369.59 to 0.23.

Table 4 Simulation parameters for Weber number sweep

Physical parameters
U=-[20, 15, 10, 8, 5, 3, 2.5, 1, 0.75, 0.5]m/s
ρ_{ink}= 1.1827e3 kg/m^3
ρ_{air}= 1.225 kg/m^3
η_{ink} = 5e-3Pa*s
η_{air} = 1.7894e-5 Pa*s

σ = 0.064N/m
g = 9.81 m/s^2
D = 50e-6 m

As mentioned above, there are three different forces playing roles in the spreading of the droplet, which are the hydrodynamic pressure, the surface tension and the viscous force, corresponding to the spreading time scale, oscillation time scale and viscous time scale. The hydrodynamic pressure is defined as ρU^2 as in Bernoulli's equation. Therefore, the three different forces can be defined as below:

$$F_p = \rho U^2 D^2;\ F_\sigma = \sigma D;\ F_{vis} = \eta U D\ ;$$

where F_p is the hydrodynamic force, F_σ is the surface tension force and F_{vis} is the viscous force.

Hydrodynamic force comes from the kinetic energy, surface tension force comes from the surface tension energy while the viscous force dissipates energy. During the droplet spreading, the hydrodynamic force tries to deviate the droplet from the equilibrium shape and the surface tension force strives to restore the droplet shape to its equilibrium shape. Without viscous force, the energy will be transferred between kinetic energy and surface energy. However, the viscous force will dissipate the kinetic energy and the droplet will come to equilibrium. So during the droplet impact, if the hydrodynamic force is larger than surface tension force, the droplet will deform and the kinetic energy will be transferred to surface energy and dissipated by the viscous force and therefore the hydrodynamic force will reduce until it becomes smaller than the surface tension force. Then, the droplet will be relaxed back to its equilibrium shape under the surface tension force and in the meantime the surface energy will be transferred to kinetic energy, which will result in hydrodynamic force and if it's still larger than the surface tension force, this process will be repeated until the kinetic energy is dissipated.

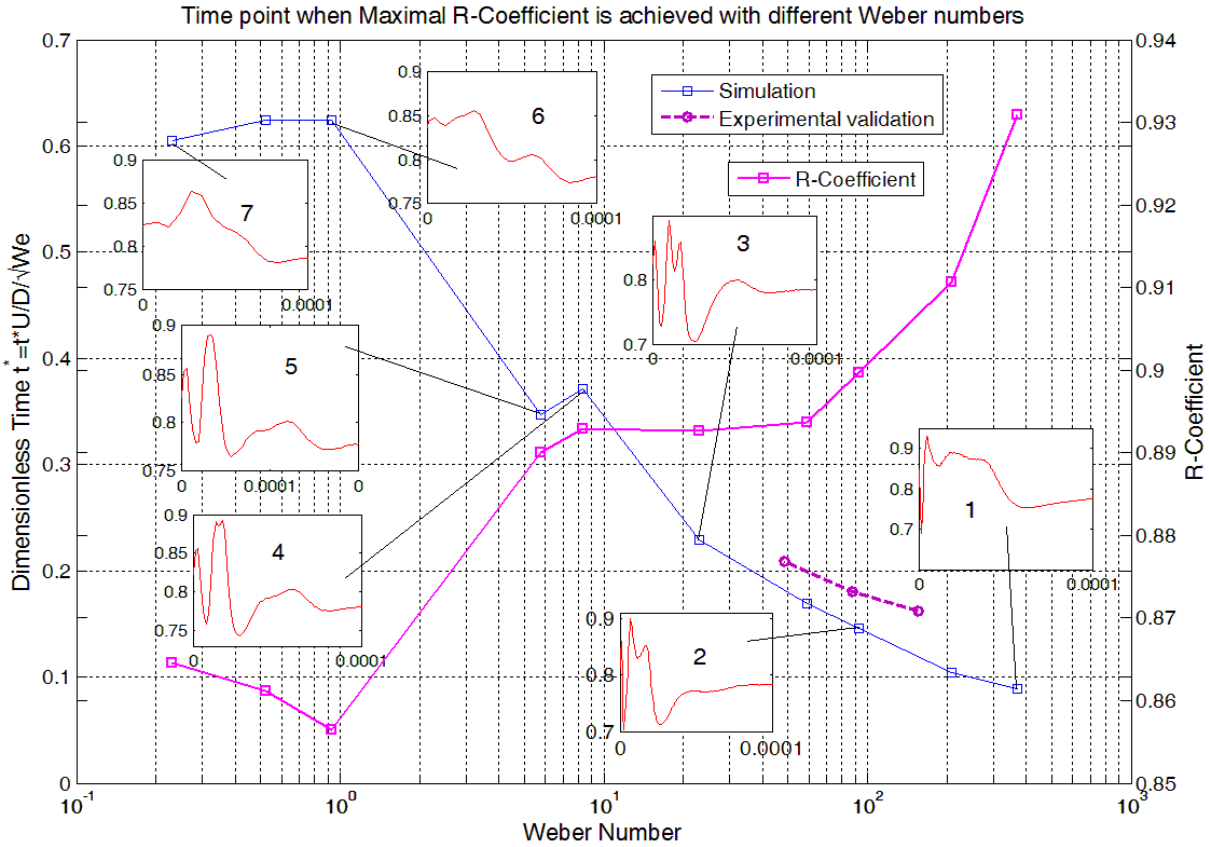

Figure 12 Time point when maximum R-coefficient is achieved with different We number

With the droplet impact process in mind, we can define the dimensionless numbers in another way as the ratios of the three forces:

$$We = \frac{F_p}{F_\sigma};\ \ Re = \frac{F_p}{F_{vis}};\ \ \ Oh = \frac{\sqrt{We}}{Re}$$

This definition gives more physical sense of Weber number for droplet impact and therefore can help with the analysis of effects of Weber number.

The simulation results are shown in Figure 12. The changes of the maximum R-Coefficient time point and its amplitude with respect to Weber number are plotted and the shape evolutions of representative time points are plotted on top.

It can be seen that when Weber number decreases from its maximum value, the time required to achieve the maximum R-coefficient increases, and the maximum R-coefficient decreases when the Weber number decreases. The reason is because the droplet is deformed more and faster with larger Weber numbers since the difference between hydrodynamic force and surface tension force is larger.

When the Weber number approaches 10 (10^1), the maximum R-coefficient does not change much in this transition area since the hydrodynamic force and the surface tension force influence the droplet shape around the maximum R-coefficient time point and thus the third peak surpasses the second one as shown in subplot 4. Then the two peaks merge together in this transition area as shown in subplot 5. When the Weber number becomes less than 1, the spreading process is dominated by the surface tension and thus the maximum R-coefficient time point does not vary much as shown in subplots 6 and 7.

The results are partially validated by experiments from the literature. Since very little shape data of droplet impact exists in the literature, simulations are conducted with the same parameters as the experiments in the literature [20] and the spreading factors are compared as shown in Figure 13. With the good agreements between the simulations and experiments in the early stage of the droplet spreading, the shape information of the simulations is compared with previous analysis as shown in Figure 12. As can be seen, the results agree well and the slight discrepancy could be due to the different time resolutions used in the simulations and numerical errors.

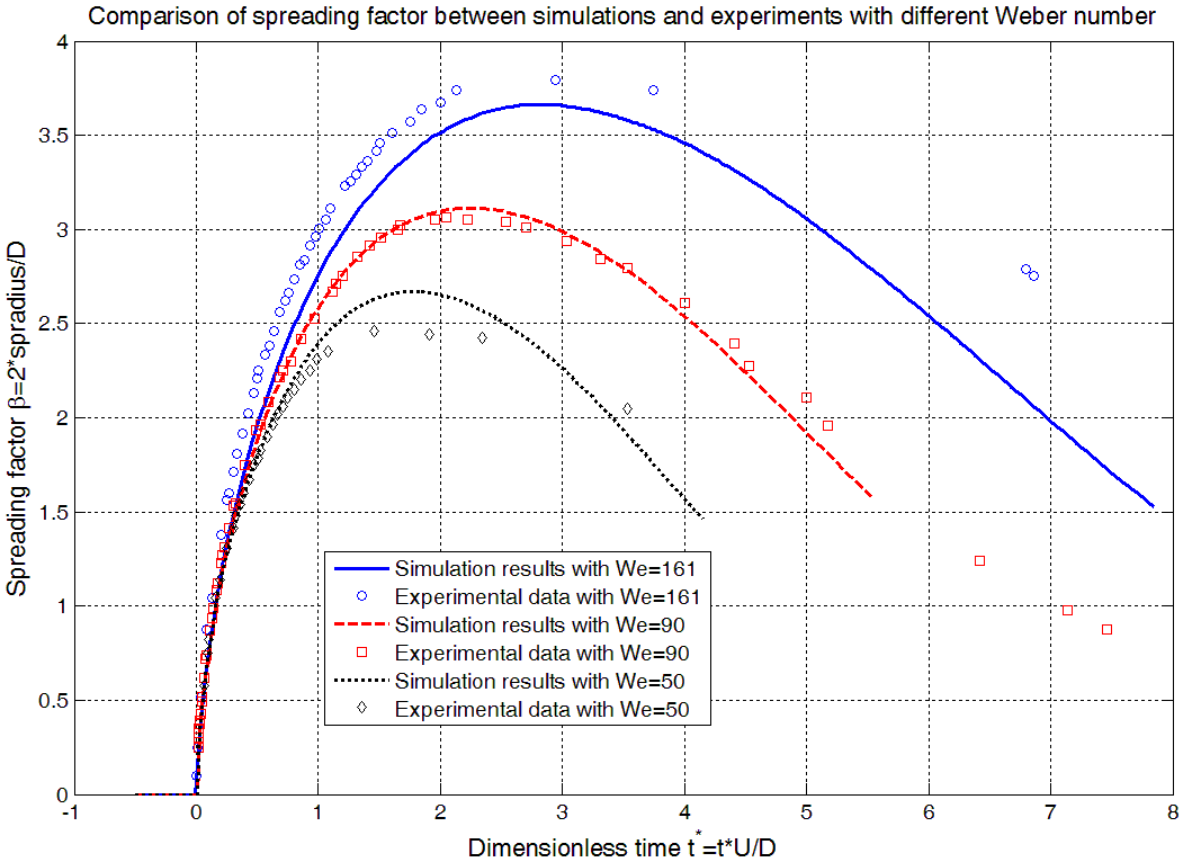

Figure 13 Comparison of spreading factor between simulations and experiments with different Weber number (experimental data comes from Fig. 6 of [20])

2. Effects of Ohnesorge number

To examine the effects of the Ohnesorge number on the droplet shape evolution, a series of simulations are performed at the conditions listed in Table 5. As can be seen, all the physical parameters are kept constant except the viscosity of the droplet, which is varied from 5e-4Pa*s to 5Pa*s uniformly on a log scale. The Weber number is kept at 100 while the Ohnesorge number ranges from 0.01 to 100.

Table 5 Simulation parameters for Ohnesorge number sweep

Physical parameters
U=-10m/s
ρ_{ink}= 1000 kg/m^3
ρ_{air}= 1.225 kg/m^3
$\eta_{ink} = 10^{\log_{10}(5e-4)+(i-1)*\log_{10}(5/5e-4)/50}$ Pa*s (i=1,2..50)
η_{air} = 1.7894e-5 Pa*s
σ = 0.05 N/m
g = 9.81 m/s^2
D = 50e-6 m

The change of the time point of maximum R-coefficient is plotted against the Ohnesorge number as shown in Figure 14. The evolution of the shape coefficient of several representative time points is plotted on top as well.

As stated above, the dimensionless numbers can be interpreted as the ratio of different time scales. To facilitate the analysis of the results, the time scales are calculated as below:

$$\tau_{spr} = \frac{D}{U} = 5e-6 \text{ sec};\ \tau_{osc} = \sqrt{\frac{\rho D^3}{\sigma}} = 5e-5 \text{ sec};\ \tau_{vis} = \frac{\rho D^2}{\eta} = [5e-7, 5e-3]\text{sec}$$

When the Ohnesorge number is small, the viscous time scale is relatively large compared with the spreading and oscillation time scales and thus the viscous effect is negligible on the early stage of the spreading. Since the maximum R-coefficient always come at early stage of the spreading as shown before, the maximum R-coefficient time point is nearly constant when Ohnesorge number is small as shown in subplots 1 and 2 in Figure 14 while the maximum R-coefficient still decreases due to the increasing dissipation of the kinetic energy as the Ohnesorge number increases.

When the viscous time scale is getting smaller at subplot 3, where $\tau_{vis} = 1.046e-4$ sec , the viscous force starts to affect the peak of the maximum shape coefficient and the later peak replaces the earlier peak becoming the maximum. As the viscous time keeps decreasing, the close-seated two peaks are merged into one peak as shown from subplots 3 to 5.

When the viscous time scale approaches the oscillation time scale (i.e. Oh=1), the maximum R-coefficient has an abrupt drop and is achieved when the droplet first hits the substrate as shown in subplot 6. When the viscous time scale is getting close to the spreading time scale at subplot 7 (where $\tau_{vis} = 1.37e-5$sec), all the oscillations are damped out and the droplet shape just goes from the equilibrium shape in the air (i.e. a sphere) to the equilibrium shape on the surface (i.e. a sphere cap) under the control of the surface tension force that strives to restore the droplet shape to equilibrium shape at every moment. The maximum R-coefficient is thus achieved at a much later time as shown in subplot 7. It should be noted that with Ohnesorge number larger than 1, the droplet does not deform much for its equilibrium shape and thus the R-coefficient is not good enough for manufacturing purpose.

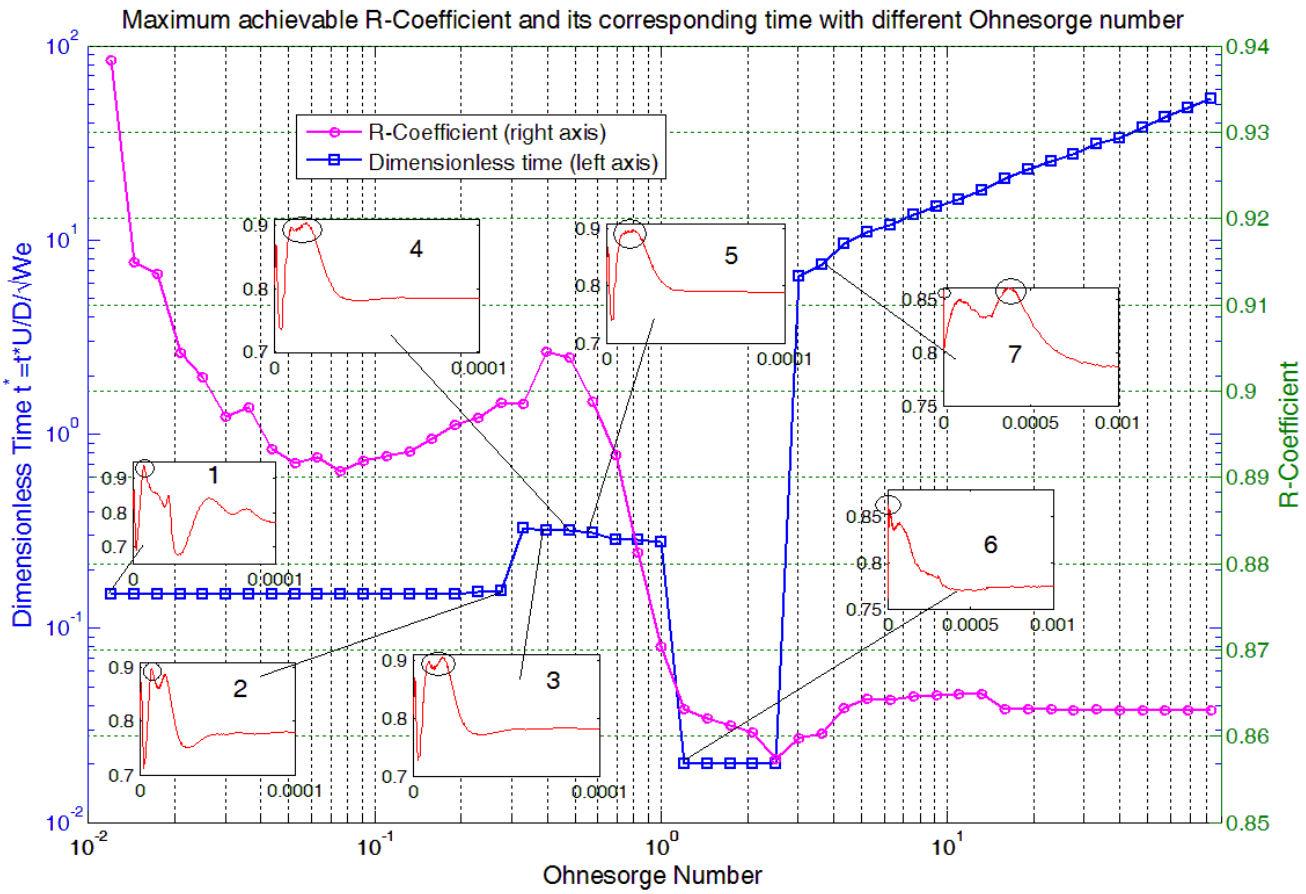

Figure 14 Time point when maximum R-coefficient is achieved with different Oh number

6. Successive droplets impact

Besides studying single droplet impact behavior on the regime map, we can also explore multiple droplet impact behaviors with the defined droplet shape coefficient (R-coefficient) to see if there is a way to improve the droplet shape without changing the impact conditions. In this section, an ideal situation of successive droplets impact is investigated. The ideal situation is where one droplet impinges on the solid surface and is frozen instantly at the moment when its shape is closest to the desired shape. Then the next droplet hits on top of the previous frozen droplet and is frozen instantly. This process is repeated for successive droplets.

The impact conditions are set to be Weber number equal to 71.42 and Ohnesorge number equal to 0.169 (or Reynolds number equal to 50) and the Froude number equal to 2.0387E5. The first droplet impingement is shown in Figure 2 and is frozen instantly when its R-coefficient reaches maximum. The second droplet impingement on top of the first frozen droplet is plotted in Figure 15. Comparing Figure 15 with Figure 2, we find that the best achievable shape is improved (i.e. the maximum R-coefficient for two successive droplets impact is larger than that of the single droplet impact).

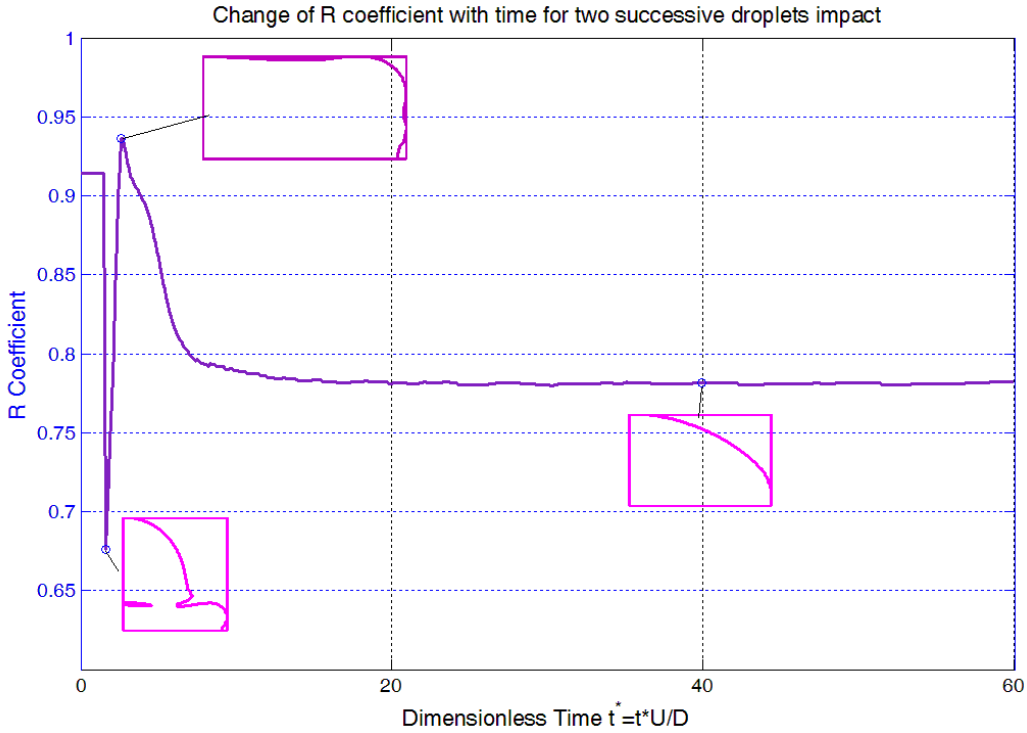

Figure 15 Change of R coefficient with time for two successive droplets impact

To further test this idea, multiple successive droplet impact simulations are conducted and the R-coefficient is plotted against the number of droplets, as shown in Figure 16. As can be seen, the shape of the droplets is getting closer and closer to the desired shape as the number of droplets increases, which suggests it is possible to optimize the manufacturing process by controlling the droplet deposition and solidification process.

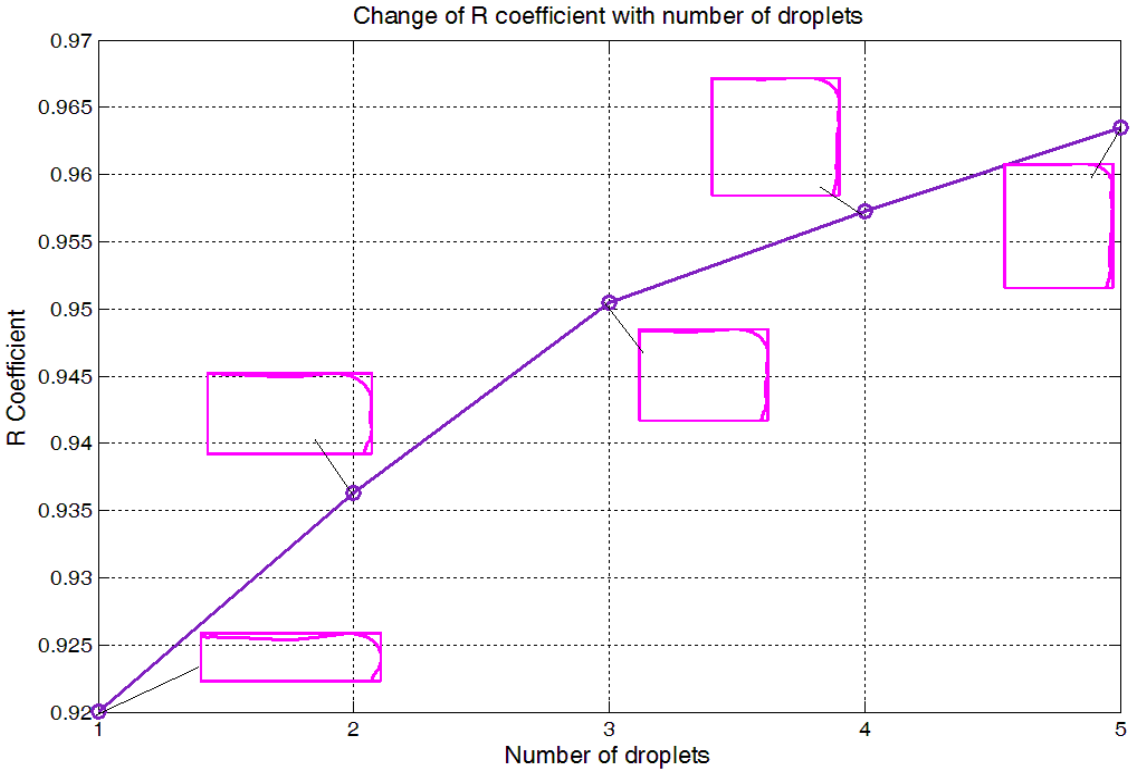

Figure 16 Change of best achievable shape coefficient with number of droplets

7. Conclusions

A shape coefficient is defined to provide more relevant information of droplets impingement for manufacturing purpose, which enables the optimization of the manufacturing process of ink-jet printing to build the desired geometry. The definition of the shape coefficient has been tested and is able to find the closest droplet shape to the desired geometry during the droplet impingement. Then a dimensionless analysis of the droplet impact is conducted and has revealed that three independent dimensionless numbers determine the droplet impact behavior. The comparison between the simulation results in dimensionless domain and physical domain validated the dimensionless analysis. A wide range of impact conditions on the regime map that is composed of two of the three independent dimensionless numbers (i.e. the Weber number and the Ohnesorge number) have been simulated and provided more information of the droplet impact behavior in terms of the shape coefficient. The examination of the effects of the third independent dimensionless number (i.e. the Froude number) on the droplet impact behavior is performed and it's shown that Froude number does not affect the droplet impact behavior very much under interested impact conditions, which makes it possible to conduct the droplet impact experiments in macro-scale to estimate the impact behavior in micro-scale. The close look of the effects of dimensionless numbers on the shape evolution of droplet impact reveals that the best shape can only be obtained in the early stage of the spreading and different shape evolution patterns with different Weber number and Ohnesorge number are summarized and analyzed, which show that larger Weber number and smaller Ohnesorge number give better R-coefficients. Other than the investigation of the single droplet impact behavior on the regime map, the multiple droplets impact has also been explored. An ideal situation of successive droplets impingement is examined, which shows that the droplets shape can be improved toward the desired shape by increasing the number of droplets under this ideal situation.

8. Acknowledgement

We gratefully acknowledge the U.S. National Science Foundation, through award DMI-0900322. Any opinions, findings, and conclusions or recommendations expressed in this publication are those of the authors and do not necessarily reflect the views of the National Science Foundation.

9. References

1. Worthington, A.M., *On the forms assumed by drops of liquids falling vertically on a horizontal plate.* Proc. R. Soc. London, 1876. **25**: p. 261-271.
2. Dussan, E.B., *On the spreading of liquids on solid surfaces: static and dynamic contact lines.* Annual Review of Fluid Mechanics, 1979. **11**: p. 371-400.
3. N. Nagai, and V.P. Carey. *Assessment of surface wettability and its relation to boiling phenomena.* in *Proceedings of the 2001 ASME International Mechanical Engineering Congress and Exposition.* 2001. New York, NY. USA.
4. Carey, V.P., *Liquid-vapor phase change phenomena, an introduction of vaporization and condensation processes in heat transfer equipment.* Taylor and Francis, Series in Chemical and Mechanical Engineering, 1992.
5. R. Rioboo, M. Marengo, and C. Tropea, *Time evolution of liquid drop impact onto solid, dry surfaces.* Experiments in Fluids, 2002. **33**: p. 112-124.
6. S. Schiaffino, and A.A. Sonin, *Molten droplet deposition and solidification at low Weber numbers.* Phys. Fluids, 1997. **9**(11): p. 3172-3187.
7. L. Xu, W.W. Zhang and S.R. Nagel, *Drop splashing on a dry smooth surface.* Phys. Rev. Lett., 2005. **94**: p. 184505.
8. Lei Xu, L. Barcos, and S.R. Nagel, *Splashing of liquids: Interplay of surface roughness with surrounding gas.* PHYSICAL REVIEW E, 2007. **76**: p. 066311.
9. R.E. Pepper, L. Courbin and H.A Stone, *Splashing on elastic membranes: the importance of early-time dynamics.* Phys. Fluids, 2008. **20**: p. 082103.

10. Astarita, G., *Dimensional analysis, scaling, and orders of magnitude.* Chemical Engineering Science, 1997. **52**(24): p. 4681-4698.
11. G. McHale, S. M. Rowan, and M. I. Newton, *Frenkel's method and the spreading of small sperical droplets.* J. Phys. D, 1994. **27**: p. 2619.
12. Z. Zhao, D. Poulikakos and J. Fukai, *Heat transfer and fluid dynamics during the collision of a liquid droplet on a substrate - I. Modeling.* International Journal of Heat and Mass Transfer, 1996. **39**: p. 2771-2789.
13. M. Sussman, P. Smereka, and S. Osher, *A level set approach for computing solutions to incompressible two-phase flow.* J. Comp. Phys., 1994. **114**: p. 146-159.
14. F.H. Harlow, and J.E. Welch, *Numerical calculation of time dependent viscous incompressible flow of fluid with free surface.* Physics of Fluids, 1965. **8**: p. 2182-2189.
15. M. Bussmann, J. Mostaghimi and S. Chandra, *On a three-dimensional volume tracking model of droplet impact.* Physics of Fluids, 1999. **11**: p. 1406-1417.
16. P. Yue, C. Zhou, J.J. Feng, C.F. Olliver-Gooch, and H.H. Hu, *Phase-field simulations of interfacial dyanmics in viscoelastic fluids using finite elements with adaptive meshing.* J. Comp. Phys., 2006. **219**: p. 47-67.
17. Wenchao Zhou, Drew Loney, Andrei G. Fedorov, F. Levent Degertekin, David W. Rosen. *Impact of polyurethane droplets on a rigid surface for ink-jet printing manufacturing*. in *Solid Freeform Fabrication Symposium 2010.* 2010. Austin, TX.
18. Dengsheng Zhang, Guojun Lu, *Review of shape representation andd escription techniques.* Pattern Recognition, 2004. **37**(1): p. 1-19.
19. Sartomer. *Sartomer Product Detail*. [cited 2011; Available from: http://www.sartomer.com/prodselectdetail.asp?apid=1&plid=1&sgid=4&prid=SR351.
20. Sikalo, S., et al., *Analysis of impact of droplets on horizontal surfaces.* Experimental Thermal and Fluid Science, 2002. **25**: p. 503-510.